

## REVIEW

# Toward large-scale, ordered and tunable Majorana-zero-modes lattice on iron-based superconductors

To cite this article: Geng Li *et al* 2024 *Rep. Prog. Phys.* **87** 016501

View the [article online](#) for updates and enhancements.

## You may also like

- [On the conclusive detection of Majorana zero modes: conductance spectroscopy, disconnected entanglement entropy and the fermion parity noise](#)  
Arnav Arora, Abhishek Kejriwal and Bhaskaran Muralidharan
- [Frustration-free Hamiltonians supporting Majorana zero edge modes](#)  
Sania Jevtic and Ryan Barnett
- [Combating quasiparticle poisoning with multiple Majorana fermions in a periodically-driven quantum wire](#)  
Raditya Weda Bomantara and Jiangbin Gong

## Review

# Toward large-scale, ordered and tunable Majorana-zero-modes lattice on iron-based superconductors

Geng Li<sup>1,2,3</sup> , Meng Li<sup>1,2</sup>, Xingtai Zhou<sup>1,2</sup>  and Hong-Jun Gao<sup>1,2,\*</sup> <sup>1</sup> Institute of Physics, Chinese Academy of Sciences, Beijing 100190, People's Republic of China<sup>2</sup> School of Physical Sciences, University of Chinese Academy of Sciences, Beijing 100190, People's Republic of China<sup>3</sup> Hefei National Laboratory, Hefei 230088, People's Republic of ChinaE-mail: [hjgao@iphy.ac.cn](mailto:hjgao@iphy.ac.cn)

Received 3 April 2023, revised 19 September 2023

Accepted for publication 14 November 2023

Published 28 November 2023

**Abstract**

Majorana excitations are the quasiparticle analog of Majorana fermions in solid materials. Typical examples are the Majorana zero modes (MZMs) and the dispersing Majorana modes. When probed by scanning tunneling spectroscopy, the former manifest as a pronounced conductance peak locating precisely at zero-energy, while the latter behaves as constant or slowly varying density of states. The MZMs obey non-abelian statistics and are believed to be building blocks for topological quantum computing, which is highly immune to the environmental noise. Existing MZM platforms include hybrid structures such as topological insulator, semiconducting nanowire or 1D atomic chains on top of a conventional superconductor, and single materials such as the iron-based superconductors (IBSs) and 4Hb-TaS<sub>2</sub>. Very recently, ordered and tunable MZM lattice has also been realized in IBS LiFeAs, providing a scalable and applicable platform for future topological quantum computation. In this review, we present an overview of the recent local probe studies on MZMs. Classified by the material platforms, we start with the MZMs in the iron-chalcogenide superconductors where FeTe<sub>0.55</sub>Se<sub>0.45</sub> and (Li<sub>0.84</sub>Fe<sub>0.16</sub>)OHFeSe will be discussed. We then review the Majorana research in the iron-pnictide superconductors as well as other platforms beyond the IBSs. We further review recent works on ordered and tunable MZM lattice, showing that strain is a feasible tool to tune the topological superconductivity. Finally, we give our summary and perspective on future Majorana research.

Keywords: Majorana zero mode, STM/S, iron-based superconductors, topological bandstructure, strain

\* Author to whom any correspondence should be addressed.  
Corresponding Editor: Dr Fuchun Zhang

## 1. Introduction

Majorana fermion was named after the Italian physicist Ettore Majorana, who predicted this particle in 1937 [1]. The particle is interesting in that its antiparticle is itself. The search for Majorana fermion has never stopped since then. For example, neutrino has been proposed to be a possible candidate hosting Majorana nature [2]. However, the experimental evidence to confirm this, the neutrinoless double-beta decay in which two neutrinos annihilate each other, has not been observed yet [3]. In crystals, the motion of electrons is restricted by the crystal symmetry. As a result, it is possible that in certain materials, the rule of electron collective behavior mimics that of the Majorana fermions, giving rise to Majorana quasiparticles [4, 5].

Majorana zero modes (MZMs) are a typical type of Majorana quasiparticles. Different from the Majorana fermions which live as free particles in three-dimensional (3D) space following Fermi–Dirac statistics, MZMs exist in pairs in lower dimensions (e.g. two-dimensional (2D) and one-dimensional (1D)) following non-abelian statistics. Exchange of MZMs creates braids in e.g.  $(2 + 1)D$  which could be used for topological quantum computation [6]. The exciting fact of using MZMs as building blocks for topological qubits is that the topologically protected MZMs can be spatially distant from their partners, and thus the computing is immune to local environmental noise [7–9].

Many theoretical models have been proposed to support MZMs. Due to the intrinsic particle–hole symmetry of MZM, a straightforward host is the superconductors, in which quasiparticles are superpositions of electrons and holes. Early attempts mainly focused on superconductors with  $p$ -wave pairing. In 1990, Moore and Read showed that the ‘Pfaffian’ wavefunctions of the fractional quantum Hall state supports non-abelian anyons [10]. This wavefunction was then found to be akin to the pair wavefunction in spinless 2D  $p$ -wave superconductor [11]. In 2001, Ivanov demonstrated that MZM excitation exists in the half-quantum vortex of a  $p$ -wave superconductor [12]. Kitaev constructed a toy model showing that unpaired Majorana bound states exist at the ends of a 1D spinless chain [13].

Despite the theoretical progress, the  $p$ -wave superconductors are rarely seen in nature. Possible candidates include  $Sr_2RuO_4$  [14–16] and  $UTe_2$  [17, 18], yet the decisive evidence supporting  $p$ -wave pairing is still lacking [19]. To that, theorists turned their attention to constructing heterostructures using more practical materials. In 2008, Fu and Kane proposed that a normal  $s$ -wave superconductor in proximity to a 3D topological insulator supports MZM inside the vortices [20]. Later, Lutchyn *et al* showed that MZMs can also be created in semiconductor nanowire/superconductor heterostructures [21, 22]. Nadj-Perge *et al* suggested magnetic non-collinear structures in proximity to an  $s$ -wave superconductor serves as potential MZM platform [23–26].

Different experimental techniques were utilized to explore the platforms hosting topological superconductivity. For example, non-local transport and magnetism experiments by physical property measurements system (PPMS) provide information about the existence of superconductivity and non-trivial topology [27–29], which produce topological superconductivity and MZMs can be found at the topological defects. Angle-resolved photoemission spectroscopy (ARPES) verifies the presence of topological surface states in superconductors [30–32]. Muon spin rotation spectroscopy has been utilized to probe the intrinsic magnetic field of the samples, which thus provides information of the pairing symmetry of superconductors [33–36]. The non-local measurement techniques such as PPMS are important in Majorana research since the spatial non-locality protects MZMs from local perturbation and distinguishes them from the topologically trivial excitations. In addition, local probe measurements by scanning tunneling microscopy/spectroscopy (STM/S) gives direct visualization on the MZMs at the topological defects [37–42].

With the progress on both theoretical and experimental sides, heterostructures by placing an  $s$ -wave superconductor close to 3D topological insulators [38, 43], large spin–orbit coupling (SOC) nanowires [27, 44], and magnetic atomic chains [37, 45, 46] and islands [47–49], have been fabricated, tested and proved to host Majorana quasiparticles. However, these heterostructures are usually challenging to make, and the defects and disorders at the interfaces cause huge obstacle in interpreting the signals [50]. In 2018, MZM was observed in iron-based superconductor (IBS)  $FeTe_{0.55}Se_{0.45}$  [39, 51–53]. IBSs have a quasi-2D structure which is stacked by metallic iron-chalcogen/pnictogen layers [54–56]. The Fermi surface of IBSs mainly consists of the  $d_{xy}$ ,  $d_{yz}$ , and  $d_{xz}$  orbitals, leading to the intrinsic multiband superconducting behavior. The advantages of this new type of MZM platform lie in the facts that it is single material and that it has higher superconducting transition temperature ( $T_c$ ) compared with the traditional  $s$ -wave superconductors [51].

Following the discovery of MZM in the vortices of  $FeTe_{0.55}Se_{0.45}$ , several IBSs including  $(Li_{0.84}Fe_{0.16})OHFeSe$  [40],  $CaKFe_4As_4$  [57] and  $LiFeAs$  [58], have been verified as platforms supporting Majorana quasiparticles. The topological defects generating such quasiparticles have also been extended to magnetic impurity induced flux [59], line defects [60] and domain walls (DWs) [61]. However, the vortices in IBSs are mostly disordered, and the yield of topological vortices which host MZMs is low. In 2022, a new milestone has been reached by the observation of ordered and tunable MZM lattice in  $LiFeAs$  [42]. These discoveries make IBSs promising candidates in Majorana research.

There have been several comprehensive reviews and articles regarding the topological superconducting materials [36], DW fermions [62], and MZMs in the vortices [52, 63] and low-dimensional systems [64, 65]. While these works provide detailed review from the material synthesis to MZM

characterization, a systematic review of the state-of-the-art local probe measurements on MZMs and a comparison of different MZM-hosting platforms are necessary. In this review, we will focus on the STM/S studies of the MZMs in different platforms. We start with reviewing the iron-chalcogenide superconductors. Three different platforms, including bulk  $\text{FeTe}_{0.55}\text{Se}_{0.45}$ , bulk  $(\text{Li}_{0.84}\text{Fe}_{0.16})\text{OHFeSe}$  and the monolayer iron-chalcogenides will be discussed and compared. Then we review the Majorana research in another IBS family, the iron-pnictides.  $\text{CaKFe}_4\text{As}_4$  and  $\text{LiFeAs}$  will be discussed in this section. After that, we give a brief review on the material platforms besides the IBSs in section 4. The recent observation of ordered and tunable MZM lattice will also be reviewed in a separate section. Finally, we provide a perspective on future Majorana research based on the local probe measurements.

## 2. MZM in iron-chalcogenide superconductors

Iron-selenide  $\text{FeSe}$  was identified as a superconductor in 2008 with  $T_c = 8$  K [66]. It crystallizes in a tetragonal phase, and belongs to the  $P4/nmm$  space group (figure 1(a)). Since then, different superconductors with the backbone iron-chalcogen layers have been synthesized, leading to a new class of high- $T_c$  superconductors, namely the iron-chalcogenides [67]. The iron-chalcogenides received extensive interest since they are ideal platforms to investigate exotic physical phenomena such as the superconductivity, nematicity [68–70] and the Fulde–Ferrell–Larkin–Ovchinnikov state [71, 72] and the competition among them. In particular,  $T_c$  in monolayer  $\text{FeSe}$  grown on  $\text{SrTiO}_3$  (STO) increases to above 50 K [73], driving further effort into pushing the transition temperature to a higher limit.

### 2.1. MZM in bulk $\text{FeTe}_{0.55}\text{Se}_{0.45}$

Thanks to the multiband nature, the IBSs have later attracted physicists’ eyes from a more intriguing aspect—topology. The  $p$  orbital of the chalcogen/pnictogen and the  $d$  orbital of the iron cross and hybridize, leading to rich topological properties in these materials. Hao and Hu investigated the effect of spin–orbit interaction and the substrate of monolayer  $\text{FeSe}$  grown on STO, and proposed that robust topological phases could coexist with superconductivity [74, 75]. Wang *et al* proposed the existence of Dirac surface state in the topologically nontrivial compound  $\text{FeTe}_{0.5}\text{Se}_{0.5}$ , which was confirmed by ARPES measurements [76]. On the one hand, the substitution of Se with Te in  $\text{FeTe}_x\text{Se}_{1-x}$  enhances superconductivity over a broad range of compositions [77–79] with the maximum  $T_c = 14$  K under the optimal doping of  $x = 0.55$  [80]. On the other hand, the heavy Te atoms increases the SOC of the material, and pushes the  $p$  orbital toward the Fermi level [76]. The  $p$  orbital then hybridizes with the  $d$  orbital near the Fermi level and opens an SOC gap, inside which the topological surface state presents (figure 1(b)).

The interesting topological band structure puts  $\text{FeTe}_{0.55}\text{Se}_{0.45}$  a promising candidate for realizing MZM [81].

This type of Majorana platform has been referred to as connate [75, 82] or reciprocal-space superconducting proximity effect-induced topological superconductor [83]. The topological superconductivity on the surface serves as a consequence of conventional bulk superconductivity and the non-trivial topology on some part of the band structures (figure 1(c)). The existence of Dirac surface states in  $\text{FeTe}_{0.55}\text{Se}_{0.45}$  has been confirmed by ARPES by Zhang *et al* in 2018 [31], making the first step toward the novel Majorana platform based on IBSs. Later in the same year, Wang *et al* directly observed robust MZMs in the Abrikosov vortices of  $\text{FeTe}_{0.55}\text{Se}_{0.45}$  (figure 1) using STM/S [39]. The Te and Se atoms manifest as bright and dark dots on the surface (figure 1(d)). Under external field perpendicular to the sample surface, the Abrikosov vortices emerge (figure 1(e)) with typical sizes of  $\sim 10$  nm. The differential conductance ( $dI/dV$ ) spectrum shows strong and robust zero-bias peaks (ZBPs) at the center of the vortices, which decay without splitting toward the vortex halos. The ZBP is a well-known signature of Majorana bound states in solid materials, due to its intrinsic particle–hole symmetry. The MZM survives under 3.3 K. These works thus open up a new door in Majorana searching [31, 39].

The pioneering works were quickly followed up by other research groups. Machida *et al* reported the same ZBPs in the vortices in  $\text{FeSe}_{0.4}\text{Te}_{0.6}$  using a dilution refrigerator STM with an energy resolution as high as  $\sim 20$   $\mu\text{eV}$ , ruling out the possibility that the Majorana bound state energy is slightly off zero or is coupled with low-energy quasiparticle excitations [84]. They also found that the probability of finding ZBPs in the vortices decreases with increasing magnetic field. This phenomenon was explained by the hybridizations among the neighboring MZMs under high magnetic fields and the disordered vortex distribution [85].

Whereas the ZBP is an intrinsic character of MZM, arguments against using it as a criterion of the existence of MZM have risen from both experimental and theoretical point of view [50, 86]. As a result, new experimental technics as well as experimental designs are desperately required to build confidence in Majorana research. For example, theoretical work [87] has pointed out that the tunneling conductance from a metallic lead into an MZM would reach a plateau of the quantized conductance  $G_0 = 2e^2/h$  under sufficiently low temperatures, where  $e$  is the electron charge and  $h$  is Planck’s constant. Following this prediction, Zhu *et al* designed a tunneling experiment to look for the plateau in 2020 [41]. As depicted in figure 2(a), an MZM in a vortex is identified by an STM tip. The coupling strength between the metal tip and the MZM is adjusted by changing the tip–sample distance. For MZM, the tunneling conductance is irrelevant to the coupling strength due to the intrinsic particle–hole symmetry, and a conductance plateau should be expected as a function of the tip trajectory. For other trivial low-energy excitations, no such plateau should be observed. They did observe such a conductance plateau appearing exclusively at zero energy (figures 2(b) and (c)). The intensity of the differential conductance at different energies is plotted as a function of the tunnel barrier conductance  $G_N$  ( $G_N \equiv I_t/V_s$ , where  $I_t$  is the tunneling current and  $V_s$  is

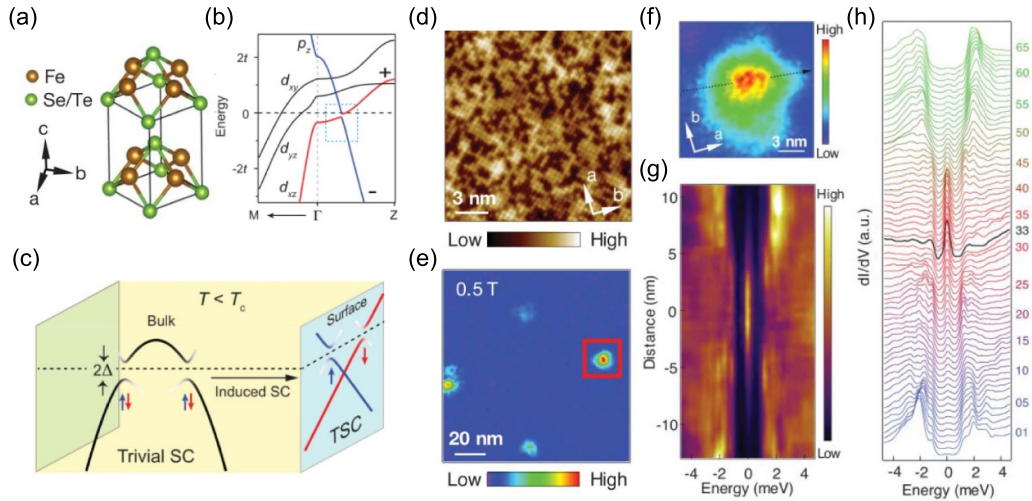


**Figure 1.** MZM in  $\text{FeTe}_{0.55}\text{Se}_{0.45}$  vortices. (a) Crystal structure of  $\text{FeTe}_{0.55}\text{Se}_{0.45}$ . (b) Calculated band structure of  $\text{FeTe}_{0.55}\text{Se}_{0.45}$  along  $\Gamma\text{M}$  and  $\Gamma\text{Z}$ . From [39]. Reprinted with permission from AAAS. (c) Schematic of superconducting states in the bulk and on the surface. From [31]. Reprinted with permission from AAAS. (d) STM topography of  $\text{FeTe}_{0.55}\text{Se}_{0.45}$ . (e) Zero-bias conductance (ZBC) map of  $\text{FeTe}_{0.55}\text{Se}_{0.45}$  under 0.5 T magnetic field. (f) ZBC map of a magnetic vortex core. (g) Intensity plot of  $dI/dV$  line-cut along the dashed arrow in (f). (h) A waterfall like plot of (f), the black curve corresponding to vortex center. From [39]. Reprinted with permission from AAAS.

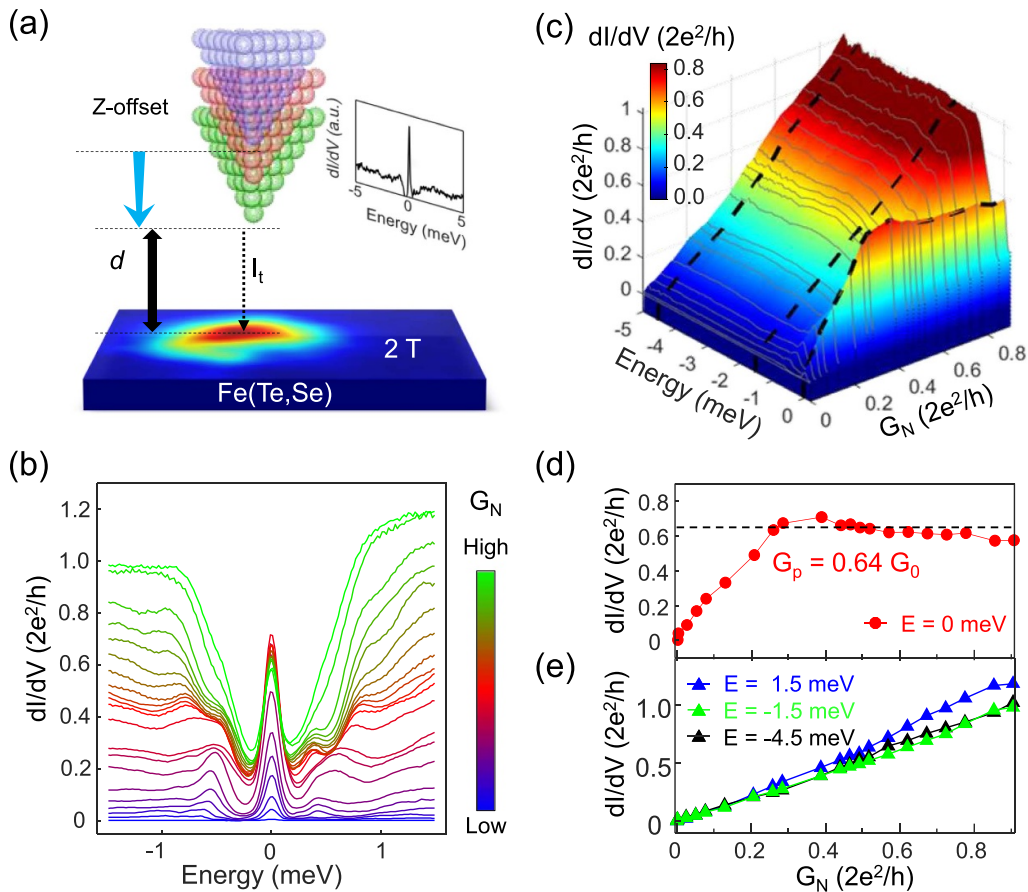


**Figure 2.** Zero-bias conductance plateau observed on  $\text{FeTe}_{0.55}\text{Se}_{0.45}$ . (a) Schematic of tunnel-coupling tunable experiment. By changing the distance between the tip and sample, the size of the tunneling junction can be altered. Inset:  $dI/dV$  spectrum measured at vortex center under 2 T. (b) An overlapping plot of  $dI/dV$  spectra at vortex center under different  $G_N$ . (c) A three-dimensional schematic diagram depicting the variation in differential conductance values with respect to changes in energy and tunnel junction. (d) Line profile of (c) along the dashed line at zero bias. (e) Line profile of (c) along the dashed lines at high bias values. From [41]. Reprinted with permission from AAAS.



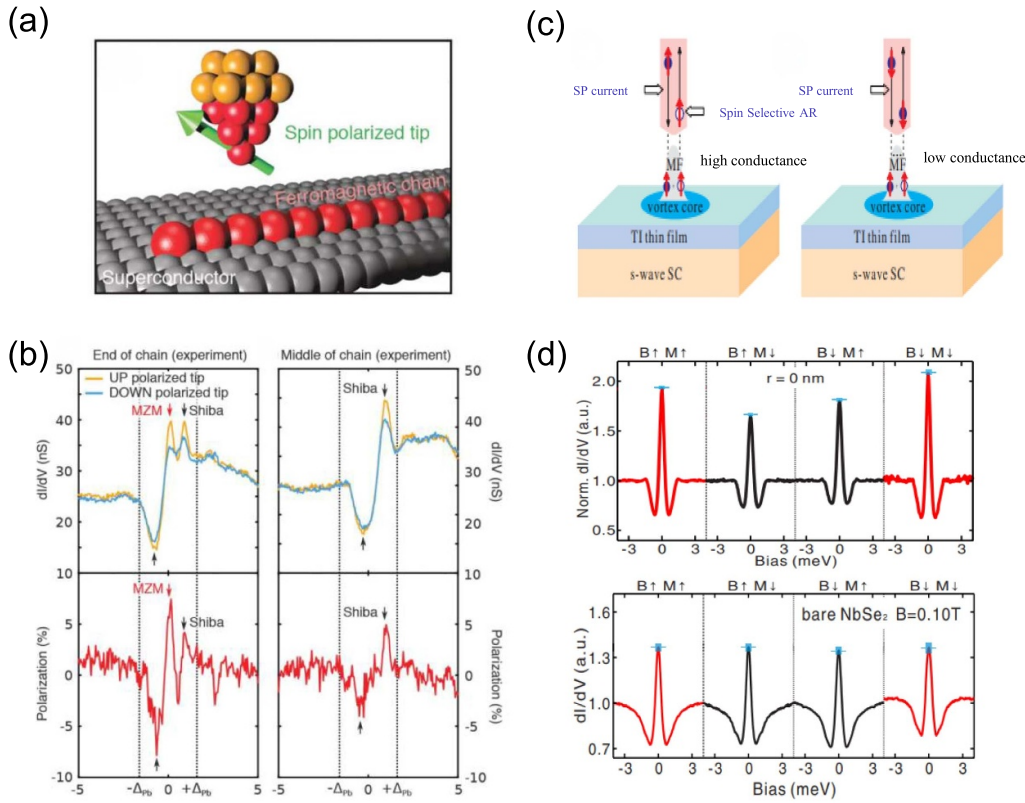


**Figure 3.** Spin polarization of MZMs at the Fe chain ends and in the vortices of  $\text{Bi}_2\text{Te}_3/\text{NbSe}_2$ . (a) Schematic of spin-polarized STM measurement. (b) Spin-polarized  $dI/dV$  spectra at the end and in the middle of the Fe chain and their corresponding polarization. From [93]. Reprinted with permission from AAAS. (c) Schematic of spin selective Andreev reflection in spin polarized STM/S at the vortex center hosting an MZM. (d) Upper panel:  $dI/dV$  spectra at the vortex center measured with a spin-polarized tip. Lower panel:  $dI/dV$  spectra on the bare  $\text{NbSe}_2$  surface measured with a spin-polarized tip. Reprinted (figure) with permission from [43], Copyright (2016) by the American Physical Society.

the set point voltage), which describes the tip–sample distance. The intensity of the zero-bias conductance reaches a plateau of about  $0.64 G_0$  (figure 2(d)). As a comparison, the differential conductances at 1.5 mV and 4.5 mV increase monotonically with increasing  $G_N$ . The observation of a conductance plateau at zero energy corroborates the particle–hole symmetry nature of MZM [41].

Very recently, Ge *et al* introduced local shot noise spectroscopy into MZM study [88]. Their experimental technique allows measurement of the effective charge of the tunneling charge carrier, and is therefore capable of distinguishing processes such as Andreev reflection (with effective charge  $q^* = 2e$ ) from normal tunneling ( $q^* = e$ ). They excluded the observed zero-energy bound states as Yu–Shiba–Rusinov (YSR) states [89–91]. However, the current state-of-the-art was not capable of unambiguously distinguishing MZM from the trivial Caroli–de-Gennes–Matricon (CdGM) bound states [92]. Another important character of MZM is the spin polarization (figure 3(a)) [86]. The spin-polarized STM/S experiments were taken on several MZMs platforms including  $\text{Bi}_2\text{Te}_3/\text{NbSe}_2$  [43], Fe chain on Pb substrate [93], and Fe atom on  $\text{FeTe}_{0.55}\text{Se}_{0.45}$  [94]. Either Fe-coated tip or bulk Cr tip were implemented to detect the spin signal. Pronounced spin-polarized signal were detected in both Fe chains ends

(figure 3(b)) and vortex cores of  $\text{Bi}_2\text{Te}_3/\text{NbSe}_2$  (figures 3(c) and (d)), distinguishing MZM from the trivial in-gap states happened to locate at zero energy [43, 93]. However, in spite of these progresses, more decisive experimental evidence is needed to unambiguously settle the arguments on the MZM detection.

## 2.2. MZM in bulk $(\text{Li}_{0.84}\text{Fe}_{0.16})\text{OHFeSe}$

Apart from  $\text{FeTe}_{0.55}\text{Se}_{0.45}$ , MZMs have also been discovered in other iron-chalcogenides. Among them,  $(\text{Li}_{0.84}\text{Fe}_{0.16})\text{OHFeSe}$  crystallizes in a tetragonal phase with alternating layers of anti-PbO-type FeSe and anti-PbO-type  $\text{LiFeO}_2$  (figure 4(a)) [95]. It has a  $T_c$  of 42 K, and thus a larger superconducting energy gap [96]. In the quantum limit [97], the energies of CdGM states are integer quantized as  $E_n = n\Delta^2/E_F$  ( $n = 0, \pm 1, \pm 2, \dots$ ), where  $n$  is the eigenvalue of angular momentum,  $\Delta$  the superconducting gap, and  $E_F$  the energy of the Dirac point with respect to the Fermi level [20, 98–100]. Large gap enables detection of a ‘pure’ MZMs, which is energetically separated from the other low-energy quasiparticles.

Liu *et al* reported the observation of clean MZMs in the vortices of  $(\text{Li}_{0.84}\text{Fe}_{0.16})\text{OHFeSe}$  [40]. Similar to

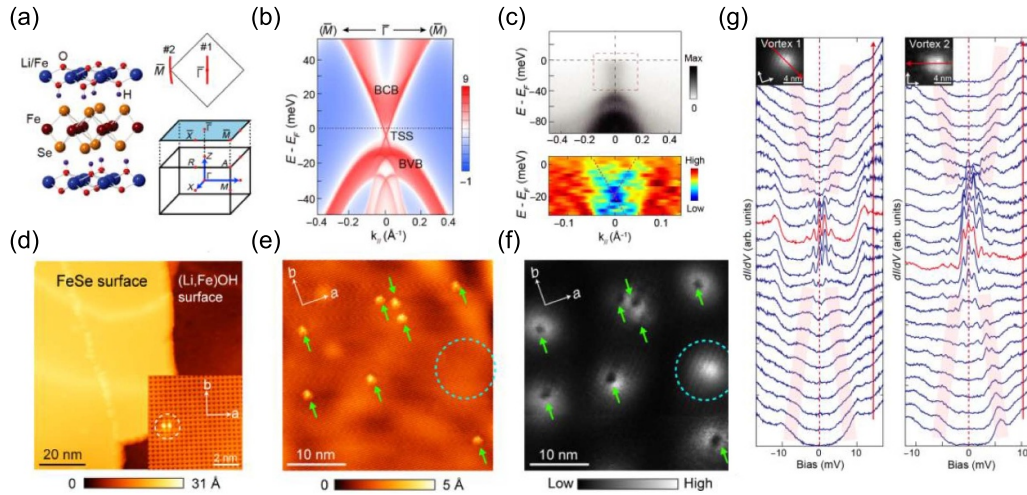


**Figure 4.** MZM in  $(\text{Li}_{0.84}\text{Fe}_{0.16})\text{OHFeSe}$  vortices. (a) Crystal structure of  $(\text{Li}_{0.84}\text{Fe}_{0.16})\text{OHFeSe}$  and schematic of Brillouin zone. (b) Calculated bulk and surface band structure along  $\Gamma$ - $\bar{M}$  direction. (c) Photoemission intensity of  $(\text{Li}_{0.84}\text{Fe}_{0.16})\text{OHFeSe}$  measured along the red line labeled #1 in (a). (d) STM topography of  $(\text{Li}_{0.84}\text{Fe}_{0.16})\text{OHFeSe}$ , inset: atomic resolved topography of FeSe surface. (e) Topography of FeSe surface. The green arrows highlight dimer-like defects. (f) ZBC map of (e). The green dashed circle highlights a free vortex. (g)  $dI/dV$  line-cuts across two free vortices. Inset: ZBC map of free vortices. Reproduced from [40]. [CC BY 4.0](https://creativecommons.org/licenses/by/4.0/).

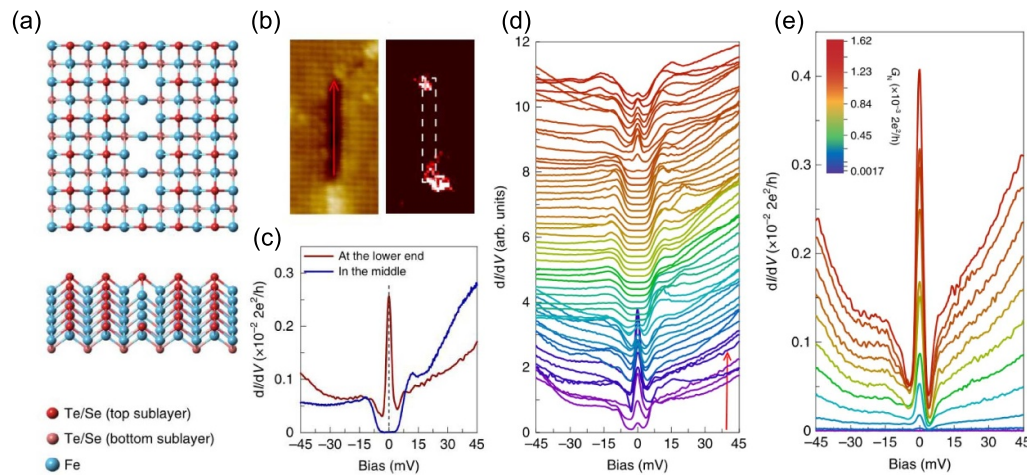


**Figure 5.** MZM in line defect of monolayer  $\text{FeTe}_{0.5}\text{Se}_{0.5}$ . (a) A schematic of line defect in monolayer  $\text{FeTe}_{0.5}\text{Se}_{0.5}$ . (b) STM topography and corresponding ZBC map of line defect. (c)  $dI/dV$  spectra at the middle and the lower end of line defect. (d)  $dI/dV$  line-cut along the red arrow indicated in (b). (e) An overlapping plot of  $dI/dV$  spectra at the top end of the line defect under different  $G_N$ . Adapted from [60], with permission from Springer Nature.

$\text{FeTe}_{0.55}\text{Se}_{0.45}$ , the dispersive Se  $4p_z$  band crosses the Fe  $3d$  bands along  $\Gamma$ - $Z$ , leading to a nontrivial band inversion that gives topological surface states under SOC (figures 4(a)–(c)). Different from  $\text{FeTe}_{0.55}\text{Se}_{0.45}$ , the Fe atoms in the  $(\text{Li}_{1-x}\text{Fe}_x\text{OH})$  layer play vital role in realizing this band topology. Due to the existence of defects on the surface (figure 4(d)), vortices may or may not pin on the surface defects (figures 4(e) and (f)). In the latter case, sharp and robust MZMs emerge at the vortex centers (figure 4(g)), together with a series of discrete CdGM states. The conductance plateau of the zero-energy bound state was later reported by the same group [101]. Given its high  $T_c$ , the  $(\text{Li}_{0.84}\text{Fe}_{0.16})\text{OHFeSe}$  can potentially serve as an ideal MZM platform.

### 2.3. MZM without an external magnetic field

While MZMs are accompanied with topological defects, physicists realized that the vortex line is not the only choice. Chen *et al* reported the observation of MZMs in the line defects of monolayer  $\text{FeTe}_{0.5}\text{Se}_{0.5}$  [60, 102]. Partially motivated by the high  $T_c$  of monolayer FeSe film grown on STO, they fabricated high quality monolayer  $\text{FeTe}_{0.5}\text{Se}_{0.5}$  by molecular beam epitaxy (MBE) method on the STO substrate, on the surface of which they observed straight atomic line defects. The origin of line defects is the absence of Te and Se atoms during the growth process (figures 5(a) and (b)). Interestingly, strong and robust ZBPs appear at both ends of the line defect, while

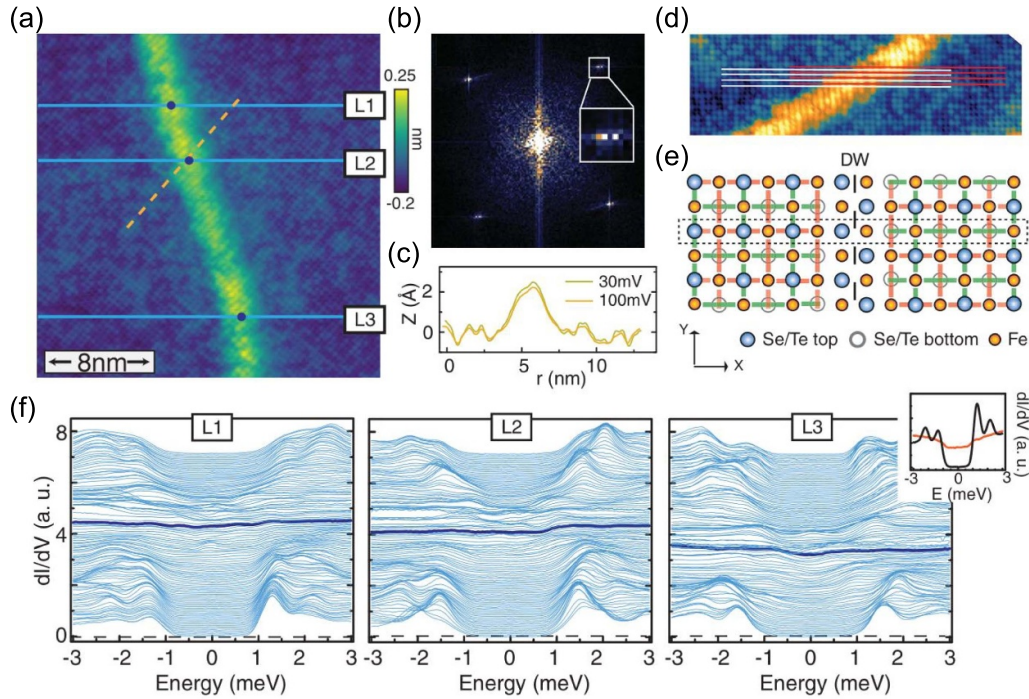


**Figure 6.** Signature of dispersing 1D Majorana modes at a  $\text{FeTe}_{0.55}\text{Se}_{0.45}$  domain wall. (a) STM topography of  $\text{FeTe}_{0.55}\text{Se}_{0.45}$ , showing a domain wall (DW). (b) Corresponding Fourier transform of (a). (c) Height line profile along the yellow dashed line in (a). (d) Zoom-in of DW, showing half-unit-cell shift across the DW. (e) Schematic of half-unit-cell shift across the DW. (f)  $dI/dV$  line-cuts along the blue lines in (a). Inset:  $dI/dV$  spectra at DW (orange) and far away from DW (black). From [61]. Reprinted with permission from AAAS.

a clean and hard gap is present at the central parts (figures 5(c) and (d)). To verify the possibility that the zero-energy peak signal originates from MZMs, they further varied the size of the tunnel junction and also observed the conductance plateau feature (figure 5(e)). By locating line defects with different lengths, the coupling between the MZMs at the chain ends changes. Notably, the surviving temperature of MZM is above 20 K.

Another example is the atomic defects on the surfaces of IBSSs. In 2015, Yin *et al* reported sharp ZBP on an interstitial iron atom residing on the surface of  $\text{FeTe}_{0.55}\text{Se}_{0.45}$  [103]. The novel bound state was later interpreted as an MZM bound to a quantum anomalous vortex (QAV) induced by the magnetic Fe atom itself given strong enough exchange coupling. This work was later extended by Fan *et al* through evaporating free and mono-iron atoms onto the  $\text{FeTe}_{0.55}\text{Se}_{0.45}$  surface at low temperature [59]. While the adsorbed iron atoms behave similar to that of the interstitial iron atoms, the exchange coupling between these atoms and the substrate can be easily adjusted by the electrostatic force from the STM tip. They thus observed a reversible transition between YSR state and Majorana bound state on the iron atoms. Compared with previously reviewed MZM platform, this platform has the potential of manipulating and braiding MZM.

#### 2.4. Dispersing Majorana modes in $\text{FeTe}_{0.55}\text{Se}_{0.45}$

So far, we have focused on the bound-state type Majorana quasiparticle manifesting as zero-energy modes at the topological

defect sites. In addition to the MZMs, another type of Majorana quasiparticle called dispersing Majorana states has also been predicted. Wang *et al* reported such a dispersing 1D Majorana state at the DW on the  $\text{FeTe}_{0.55}\text{Se}_{0.45}$  surface (figure 6(a)) [61]. Importantly, this type of DW separates the two domains with a half-lattice constant offset (figures 6(b)–(e)), which naturally provides a  $\pi$  phase shift on the two sides [104, 105]. The DW extends about 5 nm in width and has a height of about 2 Å (figure 6(c)).  $dI/dV$  line-cuts along different directions (figure 6(f)) show that the local density of states inside the superconducting gap have been filled up to a constant level, indicating the presence of linearly dispersing Majorana states at the DW. Similar phenomena in other material platforms will be reviewed in section 4.

### 3. MZM in iron-pnictide superconductors

As discussed above, the iron-chalcogenides provide reliable platforms for Majorana research. In this section, we further extend our scope into Majorana quasiparticles in iron-pnictides. Similar to iron-chalcogenides, iron-pnictide superconductors also exhibit multiband feature, and possess rich topological bandstructures [30].

#### 3.1. MZMs in $\text{CaKFe}_4\text{As}_4$

In 2020, Liu *et al* identified MZMs in  $\text{CaKFe}_4\text{As}_4$  for the first time by a combined ARPES and STM/S study [57].  $\text{CaKFe}_4\text{As}_4$  can be viewed as alternately stacked  $\text{CaFe}_2\text{As}_2$  and  $\text{KFe}_2\text{As}_2$  layers along the  $c$ -axis of the crystal [106, 107].



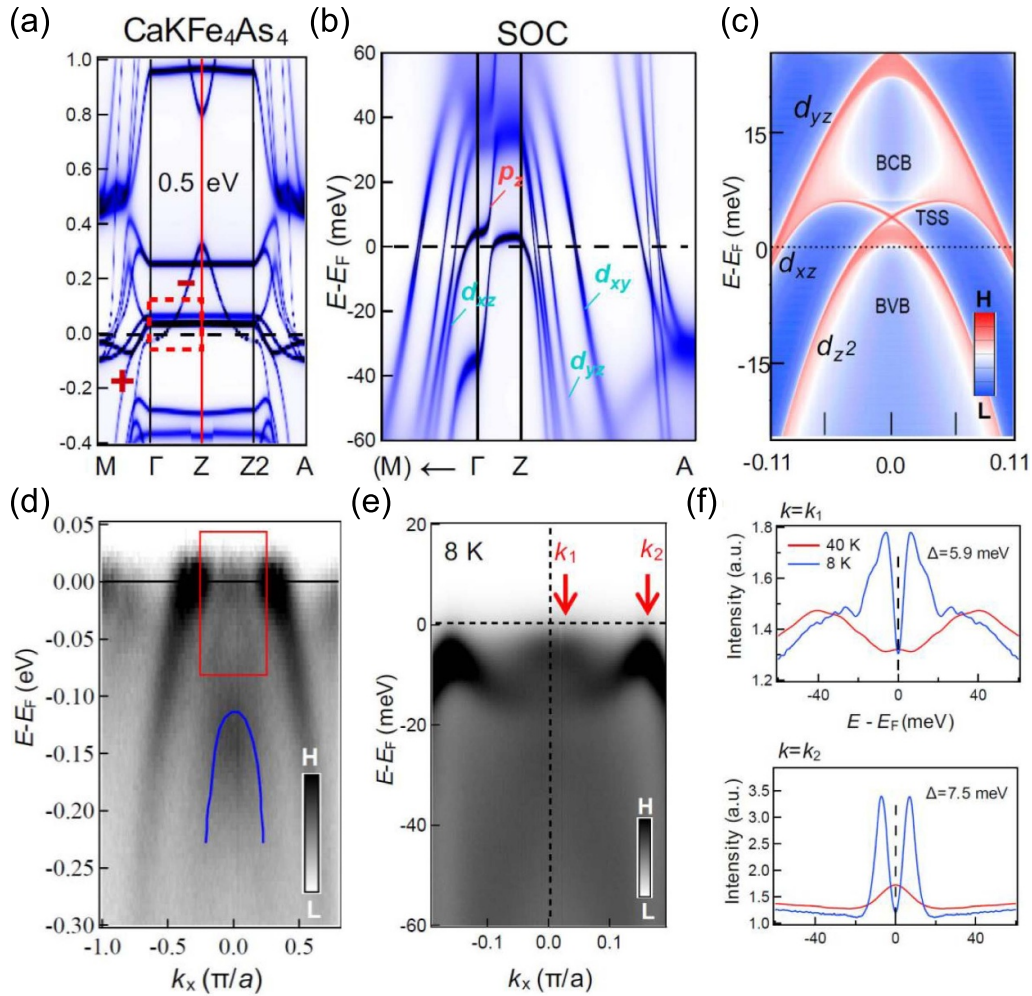


**Figure 7.** Topological surface states in  $\text{CaKFe}_4\text{As}_4$ . (a), (b) DFT + DMFT calculation results for the band structures of  $\text{CaKFe}_4\text{As}_4$ . (c) The calculated band structure projected onto the (001) surface. (d), (e) ARPES spectral intensity plots along the  $\Gamma$ -M direction on  $\text{CaKFe}_4\text{As}_4$ , showing linear dispersive band. (f) The symmetrized EDCs at the momentum points marked by the red arrows. The superconducting gap values of 5.9 meV is attributed to the topological surface bands. Reproduced from [57]. CC BY 4.0.

The alternate stacking of Ca and K ions breaks the gliding-mirror symmetry along the  $c$ -axis, leading to band folding in the Brillouin zone. Figure 7 shows the bandstructure calculated by density functional theory (DFT) plus dynamic mean field theory. Slightly different from the iron-chalcogenides discussed above, the crossings between the  $p$  orbital and the  $d$  orbitals are driven by this band folding (figure 7(a)). When SOC is considered, a topological band gap opens at the band crossing points (figures 7(b) and (c)). ARPES measurements give direct evidence to the existence of topological surface states and topological superconductivity (figures 7(d)–(f)).

The ARPES results from K-doped samples further confirms that the energy dispersion comes from topological surface state with Dirac point 20 meV above the Fermi surface. The high-resolution ARPES measurements of the superconducting states show that the two superconducting gap values are 5.9 meV at  $k_1$  and 7.5 meV at  $k_2$  (figure 7(f)). The existence of MZM signals in the vortex cores of  $\text{CaKFe}_4\text{As}_4$  is further

confirmed by STM/S measurements (figure 8). Along the white arrow in figure 8(a), the  $dI/dV$  spectra show the homogeneous superconducting gap feature under 0 T (figure 8(b)). When magnetic field is applied perpendicular to sample surface, vortices enter the sample and appear as bright spots (figure 8(c)). A pronounced ZBP can be clearly seen at the center of the vortex, together with the low-lying CdGM states, putting the system in the quantum limit (figures 8(d)–(f)). In addition, they looked into the spatial patterns of the vortex bound states (figures 8(g) and (h)). Both the MZM ( $L_0$ ) and the first-level CdGM state ( $L_{-1}$ ) show a solid-circle pattern, while the other higher energy CdGM states ( $L_{-2}$  and  $L_{-3}$ ) show hollowing patterns [108].

It is worth noting that the advantage of  $\text{CaKFe}_4\text{As}_4$  lies in two aspects. Firstly, it has  $T_c$  of 35 K, which is much higher than that of  $\text{FeTe}_{0.55}\text{Se}_{0.45}$ . Secondly, it has a much more homogeneous bulk state compared with that in  $\text{FeTe}_{0.55}\text{Se}_{0.45}$  [106].

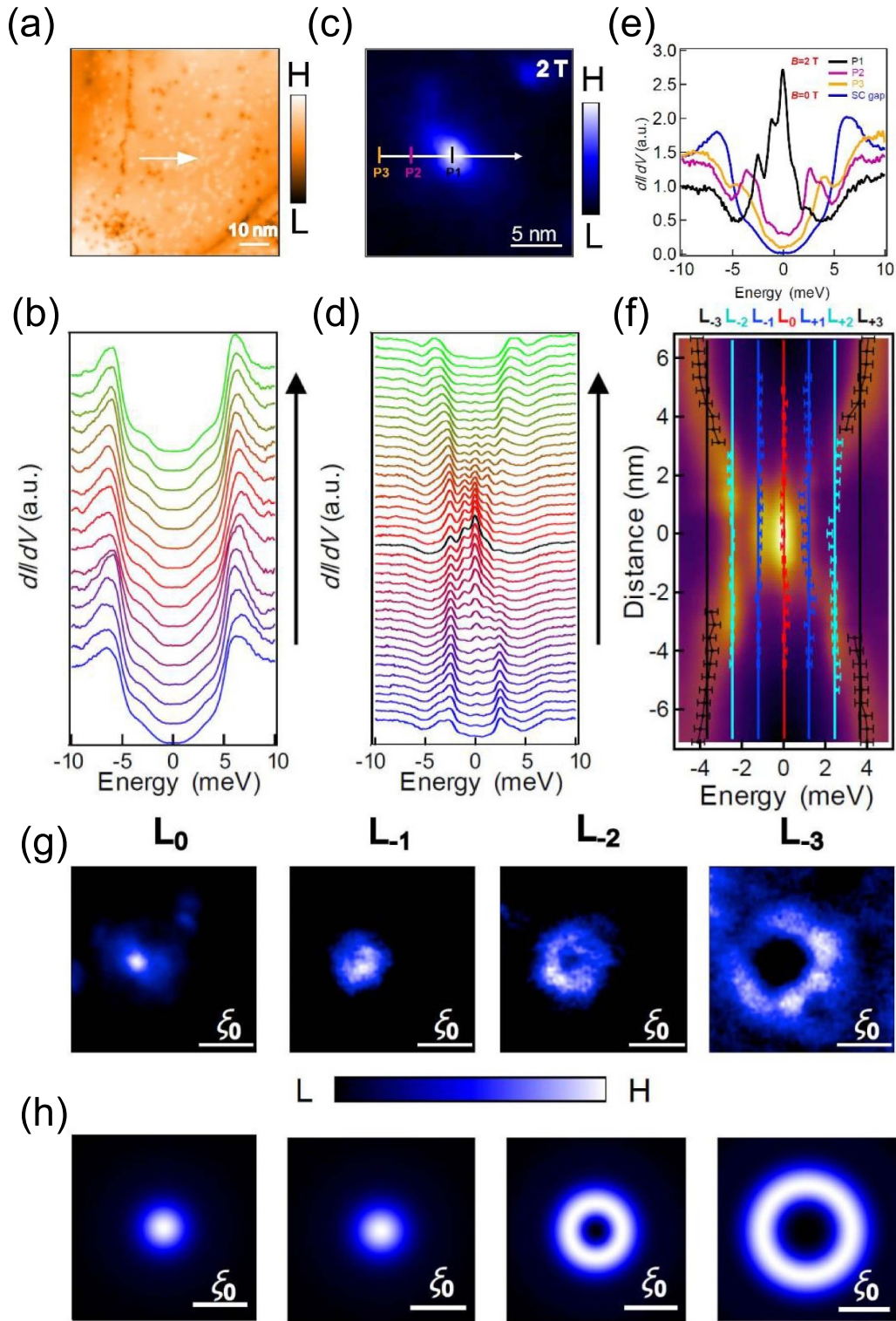


**Figure 8.** MZM in CaKFe<sub>4</sub>As<sub>4</sub> vortices. (a) STM topography of CaKFe<sub>4</sub>As<sub>4</sub>. (b) STS spectra taken along the white arrow in a. (c) Zero-bias conductance map around a vortex core. (d)  $dI/dV$  spectra along the white arrow across the vortex in c. (e) Multi-Gaussian fit for the  $dI/dV$  spectrum at the vortex center. (f) Intensity plot with the colored marked lines representing the ZBCP and discrete quantized CBSs. (g) Spatial patterns of vortex-bound states at energies corresponding to  $L_0$  (MZM),  $L_{-1}$ ,  $L_{-2}$ , and  $L_{-3}$ . (h) Numerical calculations of the two-dimensional local density of  $L_0$  (MZM),  $L_{-1}$ ,  $L_{-2}$ , and  $L_{-3}$ , respectively, based on the topological vortex core model. Reproduced from [57]. CC BY 4.0.

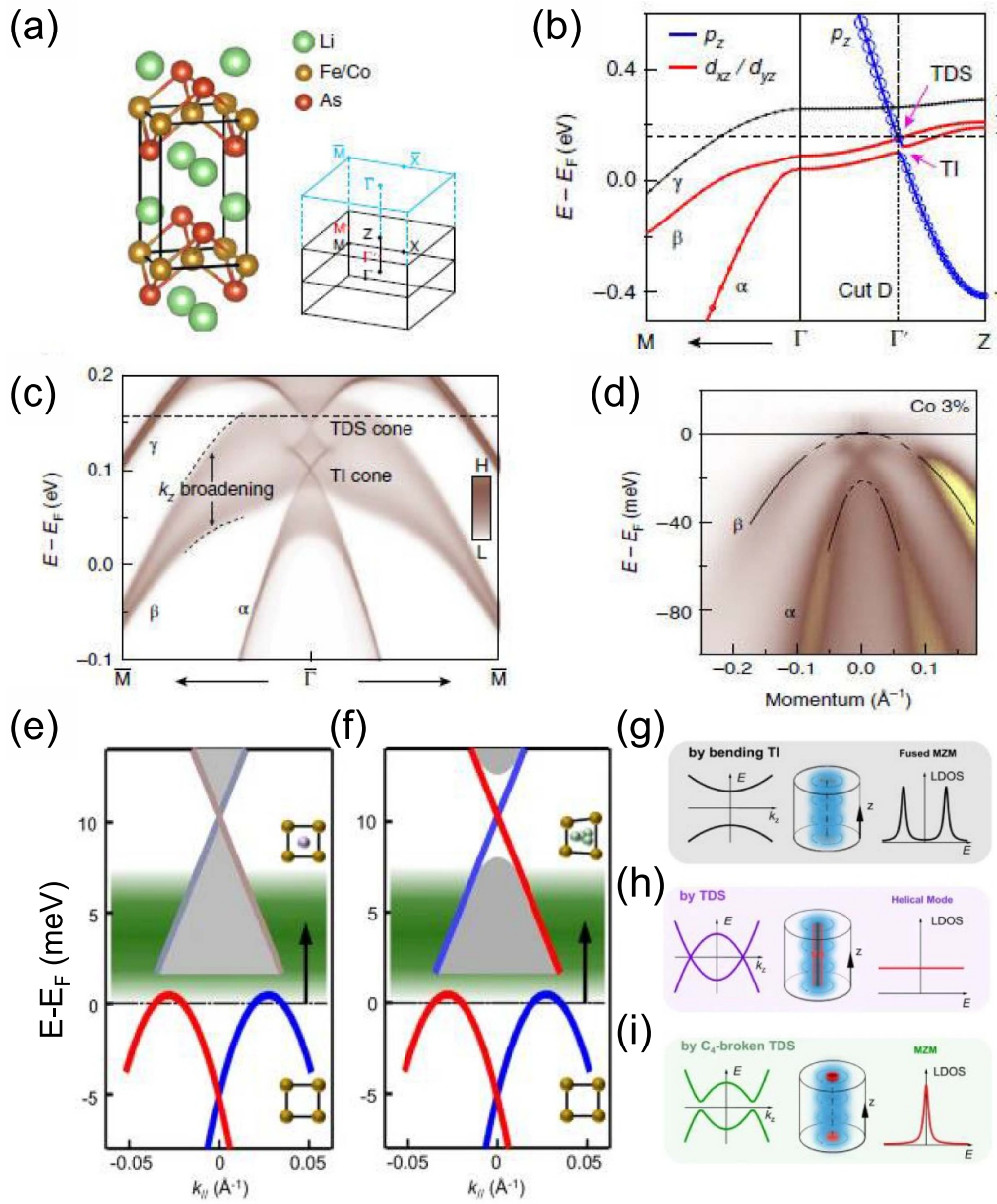


**Figure 9.** Topological band structures in LiFeAs. (a) Crystal structure and Brillouin zone of Li(Fe,Co)As. (b) LiFeAs band dispersion along  $\Gamma$ -M and  $\Gamma$ -Z. (c) (001) surface spectrum of LiFeAs. (d) ARPES intensity plot of LiFe $_{1-x}$ Co $_x$ As ( $x = 3\%$ ) at 15 K, showing TI bands. Adapted from [30], with permission from Springer Nature. (e), (f) Schematic depictions of topological band structure of LiFeAs influenced by impurities. (g)–(i) Low-energy vortex bound states (left), vortex line diagram (middle) and density spectrum of local density of states (right) without impurities (g), impurities (h) that do not destroy  $C_4$  symmetry and impurities that destroy  $C_4$  symmetry (i). Reproduced from [58]. CC BY 4.0.

### 3.2. MZMs in impurity assisted vortex in LiFeAs

Compared to CaKFe $_4$ As $_4$ , LiFeAs has a much simpler crystal structure and nonpolar cleaving surface plane [109, 110]. The lattice parameter along the  $c$ -axis is about 6.3 Å, which induces a  $p_z$  dispersion similar to that in FeTe $_{0.55}$ Se $_{0.45}$  (figure 9(a)). The crossing between  $p_z$  band and  $\alpha$  band opens the topological insulating (TI) gap where a topological surface state presents. The overlap between  $p_z$  band and  $\beta$  band is protected by  $C_4$  rotation symmetry, which does not open the energy gap and forms a 3D topological Dirac semimetal (TDS) state (figure 9(b)). Thus, multiple topological band structures exist

in LiFeAs [30]. The TDS Dirac cone lies around 10 meV above the Fermi level, while the TI Dirac cone lies 5 meV below the Fermi level (figures 9(c) and (e)). These topological band structures have been verified by ARPES measurement in the Co-doped LiFeAs sample (figure 9(d)) [30].

Surprisingly, however, early STM measurements showed no MZM signature in the vortex cores of LiFeAs in spite of the rich topological bandstructures [111]. According to the ARPES results, the TI states form Rashba-like band dispersion above the TI Dirac points and have a back bending feature (figures 9(e) and (f)). This causes the Fermi surface crossing the chiral Dirac band twice, leaving two unprotected MZMs



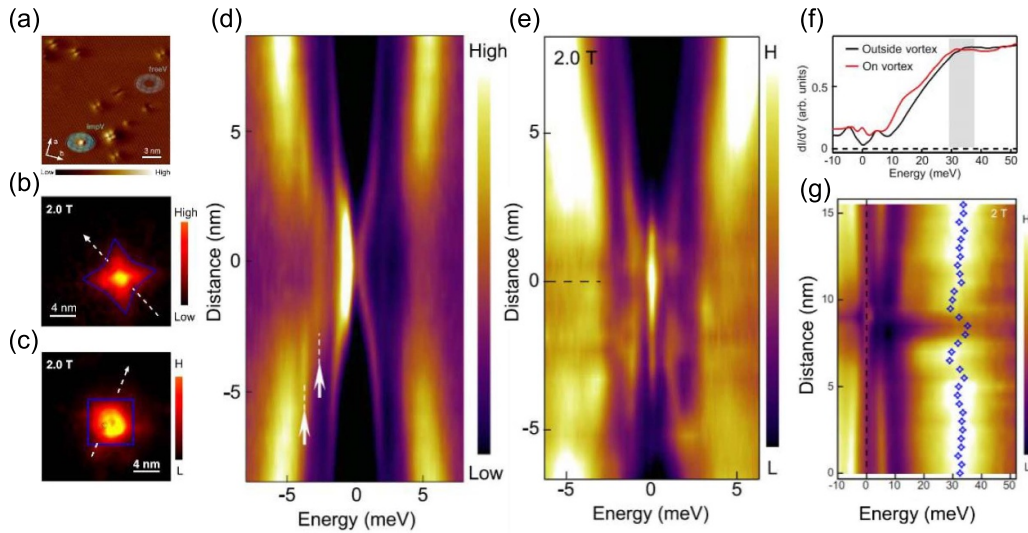


**Figure 10.** STM characterization of LiFeAs vortex states. (a) Atomic resolution STM topography of LiFeAs. (b) A zero bias conductance map around a free vortex, which exhibits star-like shape. (c) A zero bias conductance map around an impurity assisted vortex. (d)  $dI/dV$  intensity measured in the free vortex along the white dashed line indicated in (b). (e)  $dI/dV$  intensity measured under 2.0 T along the white dashed line indicated in (c). (f) Wide range  $dI/dV$  spectra measured at an impurity assisted vortex (red curve) and on a clean surface region without impurities (black curve). (g) Wide range line-cut intensity plot for an impurity assisted vortex. Reproduced from [58]. CC BY 4.0.

which quickly fused into fermionic states (figure 9(g)). It has also been proposed that the missing of MZMs is due to the coupling between the two Dirac cones [112].

Kong *et al* carried out detailed STM/S study on LiFeAs and observed reappearance of MZMs in the vortices locating nearby the large impurities (figure 10) [58]. They argued that the impurities act as local electron dopants, pushing the Fermi level up toward the TDS cone. At the same time, the impurities break the local  $C_4$  symmetry, gapping out the Dirac semimetal crossing into strong TI phase (figures 9(h) and (i)) [113, 114]. This newly formed TI Dirac cone satisfies the conditions for realizing MZMs.

#### 4. MZM in other superconducting materials

Apart from IBSs, other materials, especially some hybrid structures [86, 115–117], are proved MZM platforms by local probe measurement. One widely studied system which realizes the experimental observation of MZMs is the ferromagnetic chain/ $s$ -wave superconductor system. In 2014, Nadj-Perge *et al* deposited iron atoms on the surface of superconductor Pb(110) and found that stable MZM signals existed at both ends of the iron atomic chain [37]. In this system, the strong SOC in Pb will change the degeneracy of the  $4d$  orbital of iron, thus producing effective  $p$ -wave superconductivity. Under ideal conditions, there are always an odd number of energy bands crossing the Fermi surface, setting the system in a stable topological non-trivial state (figure 11(a)). Later, Xu *et al* constructed a 2D heterostructure by growing  $\text{Bi}_2\text{Te}_3$  layers on top of superconducting  $\text{NbSe}_2$ . They claimed that MZM appeared in the vortices in the samples with more than five quintuple layers of  $\text{Bi}_2\text{Te}_3$ , which suggested the close relationship between MZM and the topological surface states (figure 11(b)) [38]. Similar method was applied to construct other heterostructures such as  $\text{Bi}_2\text{Te}_3/\text{FeTe}_{0.55}\text{Se}_{0.45}$  [116] and

$\text{Sb}_2\text{Te}_3/\text{Fe}_{1+y}\text{Te}$  [117] showing topological superconductivity. In 2019, Palacio-Morales *et al* demonstrated the 1D Majorana dispersion mode in a 2D ferromagnet/superconductor heterostructure in which 2D iron island was grown on oxidized  $\text{Re}(0001)$  surface (figure 11(c)) [47]. Recently, Kezilebieke *et al* fabricated van der Waals heterostructures that combine 2D ferromagnets with superconductors and observed 2D topological superconductivity in the system [48]. In this system,  $\text{CrBr}_3/\text{NbSe}_2$  by MBE. Using STM/S, the characteristics of 1D Majorana edge states were revealed (figure 11(d)).

Apart from the hybrid structures, other topologically non-trivial materials, including 2M- $\text{WS}_2$  [118], 4Hb- $\text{TaS}_2$  [119],  $\text{PdTe}_2$  [120],  $\text{NiTe}_2$  [121, 122],  $\text{Bi}_2\text{Pd}$  [123],  $\text{Cu}_x\text{Bi}_2\text{Se}_3$  [124–126],  $\text{Sr}_x\text{Bi}_2\text{Se}_3$  [127–129],  $\text{Nd}_x\text{Bi}_2\text{Se}_3$  [130, 131],  $\text{SnAs}$  [132, 133],  $\text{Sn}_{1-x}\text{Sb}_x$  [134, 135],  $\text{UTe}_2$  [17, 18],  $\text{CeRh}_2\text{As}_2$  [136, 137] and  $\text{CsV}_3\text{Sb}_5$  [138–140], have been recognized as platforms hosting topological superconductivity, which greatly expanded the material library and laid a solid foundation for further application of MZMs in topological quantum computation.

#### 5. Ordered MZM lattice in LiFeAs

The works discussed in section 3.2 establishes the consensus that the chemical potential of LiFeAs has to be adjusted in order to realize MZM platform. However, impurities locate randomly inside the crystal and are not easy to control. Other methods in tuning the topological properties of LiFeAs should be developed.

Recently, Cao *et al* found 1D wrinkles on the surface of LiFeAs, which show a significant influence on the superconducting properties of the system [141]. They observed two types of characteristic wrinkles on the surface of LiFeAs (figure 12). The first type orients along  $[110]$  direction, which increases the superconducting gap. The second type orients



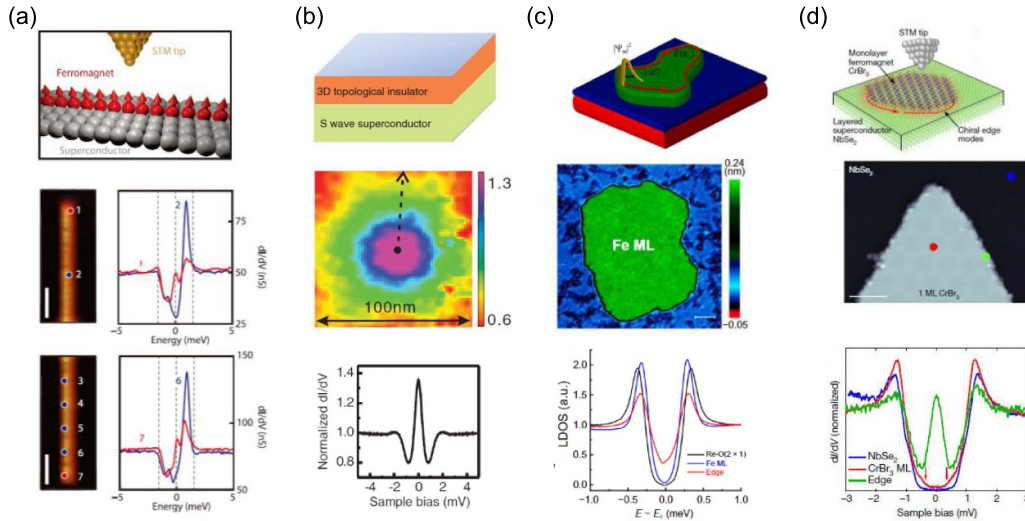


**Figure 11.** Majorana modes in other heterostructures. (a) MZM in ferromagnetic atom chain ends on superconductors [37]. Reprinted with permission from AAAS. (b) MZM in the vortices of  $\text{Bi}_2\text{Te}_3/\text{NbSe}_2$  heterostructure [38]. Reprinted (figure) with permission from [38], Copyright (2015) by the American Physical Society. (c) Majorana edge states in Fe island/ $\text{Re}(0001)\text{-O}(2 \times 1)$  heterostructure [47]. From [47]. © The Authors, some rights reserved; exclusive licensee AAAS. Distributed under a [CC BY-NC 4.0](http://creativecommons.org/licenses/by-nc/4.0/) license <http://creativecommons.org/licenses/by-nc/4.0/>. Reprinted with permission from AAAS. (d) Majorana edge states in  $\text{CrBr}_3/\text{NbSe}_2$  heterostructure [48]. Adapted from [48], with permission from Springer Nature.

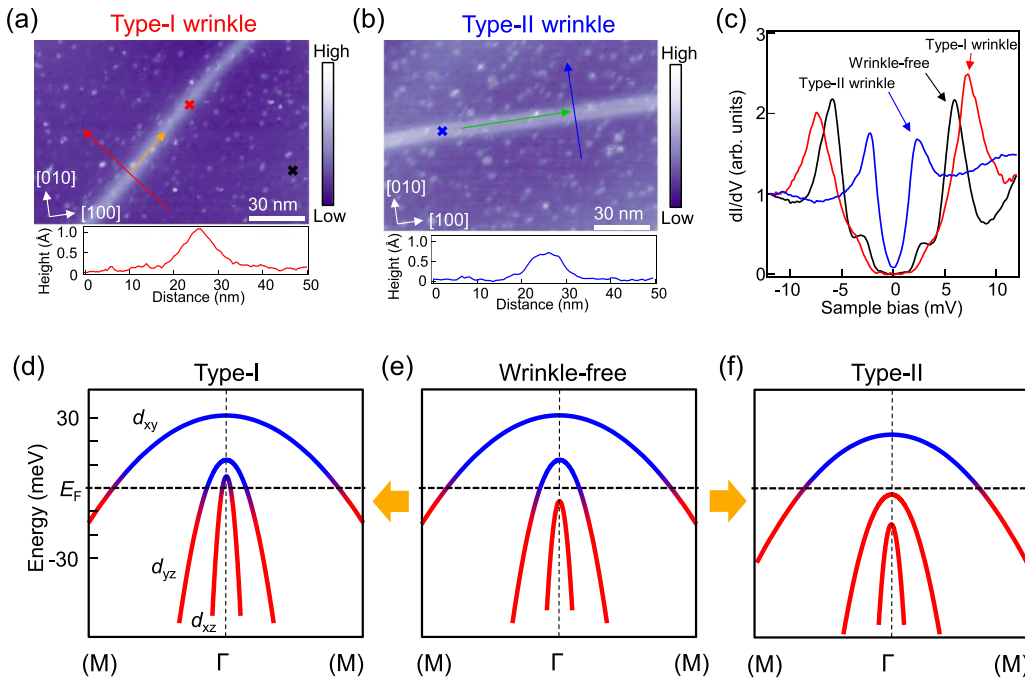


**Figure 12.** Two types of wrinkles in LiFeAs. (a) STM topography (top) and height profile (bottom) of the first type of wrinkle. (b) STM morphology (top) and height profile (bottom) of the second type of wrinkle. (c) Comparison of  $dI/dV$  spectra between the two wrinkles and the normal region. (d)–(f) Schematic diagram of tuning of LiFeAs energy band by strain in different directions. Reproduced from [141]. [CC BY 4.0](http://creativecommons.org/licenses/by-nc/4.0/).

along  $[100]$  and decreases the superconducting gap. Combined with DFT calculations, they concluded that the local strain tunes the chemical potential effectively. When strain applies along the  $[110]$ , the band top of  $d_{xz}$  will move upward and pass through the Fermi surface, increasing the electron density of states at  $\Gamma$  point. Therefore, the superconducting energy gap and superconducting transition temperature of the system will

increase. When the strain applies along  $[100]$ , both  $d_{yz}$  and  $d_{xz}$  bands sink below the Fermi surface. The uniaxial strain therefore acts an effective way to tune the chemical potential of LiFeAs [141, 142].

Motivated by this finding, Li *et al* identified a special region with natural strain in LiFeAs, which exhibits a biaxial charge density wave (CDW) structure (figure 13(a)) [42].

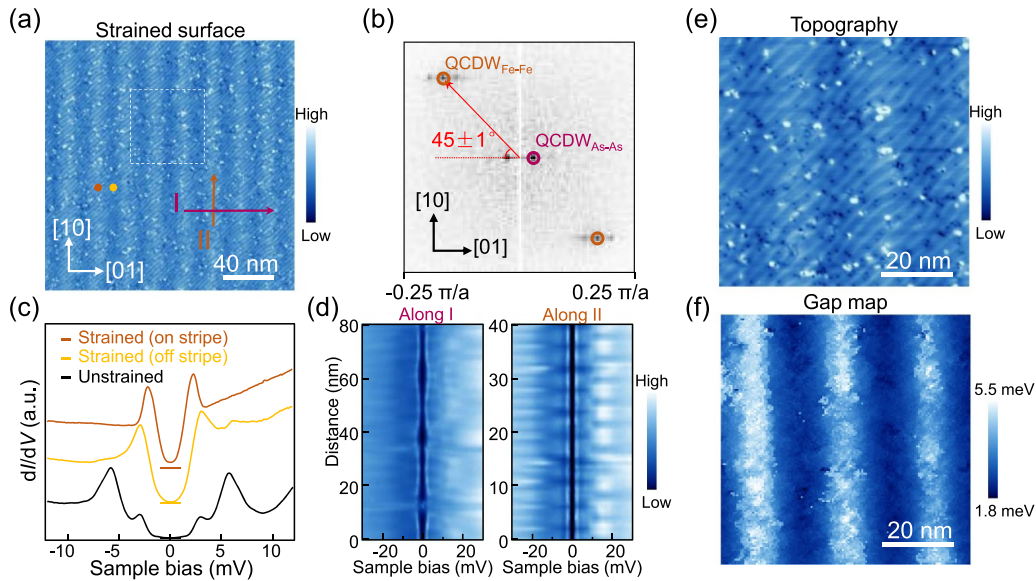


**Figure 13.** Characterization of strain-induced biaxial charge density wave in LiFeAs. (a) STM topography of large area biaxial charge density wave region. (b) Corresponding Fourier transform of (a). (c) Comparison of  $dI/dV$  spectra in different regions. (d)  $dI/dV$  intensity spectra along the arrows marked in (a). (e) STM topography of small area biaxial charge density wave region. (f) The distribution of superconducting gap value in the corresponding region of (e). Adapted from [42], with permission from Springer Nature.

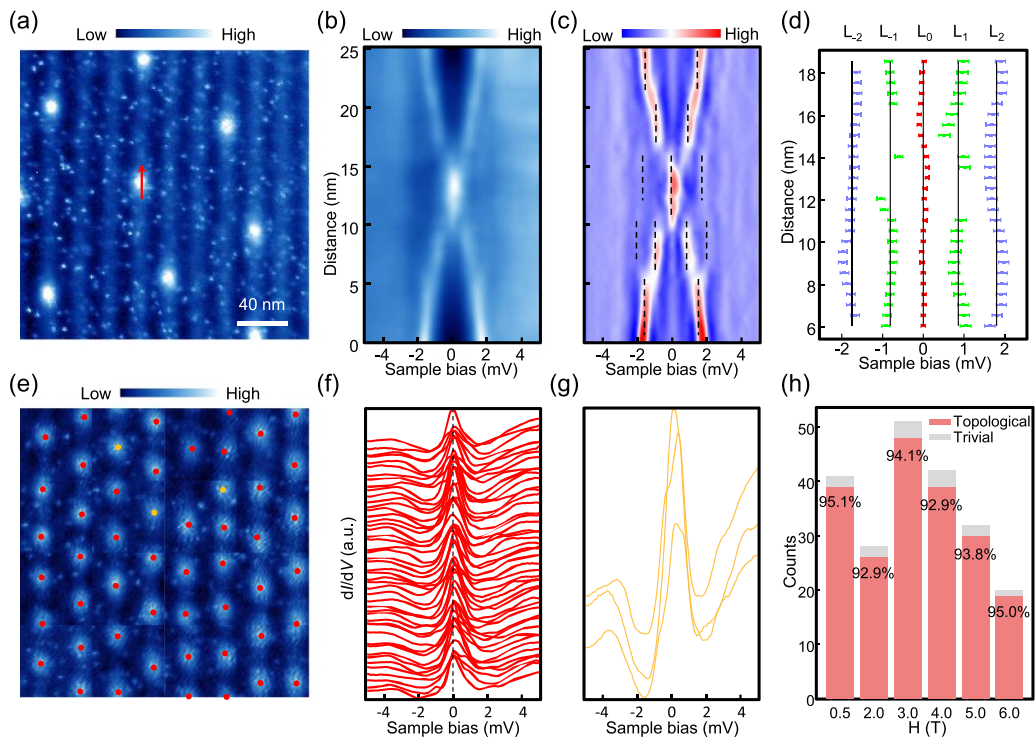


**Figure 14.** MZM in biaxial charge density wave region in LiFeAs. (a) Zero bias  $dI/dV$  map of the biaxial CDW region under 0.5 T magnetic field. (b) Intensity plot of the  $dI/dV$  spectra along the red arrow in (a). (c) Negative second derivative of (b). (d) Statistical analysis of the peak positions in (c). (e) Zero bias  $dI/dV$  map of the biaxial CDW region under 3 T magnetic field. (f) Spectra taken at the centers of the topological vortices in (e). (g) Spectra taken at the centers of the topologically trivial vortices in (e). (h) Histogram and percentage of topological vortices under different magnetic fields. Adapted from [42], with permission from Springer Nature.

The coexistence of two CDWs breaks the  $C_4$  symmetry and mirror symmetry of the crystal (figure 13(b)). They found that the biaxial CDW strongly modulates superconductivity that the superconducting gap is smaller on the bright As–As stripes than that on the dark As–As stripes (figures 13(c)–(f)).

When a magnetic field perpendicular to the sample surface is applied, the vortices appear exclusively on the bright As–As stripes where the superconducting pairing is weaker (figure 14(a)). The periodical As–As stripes thus serve as pinning centers to trap the vortex lines. Importantly, MZMs and

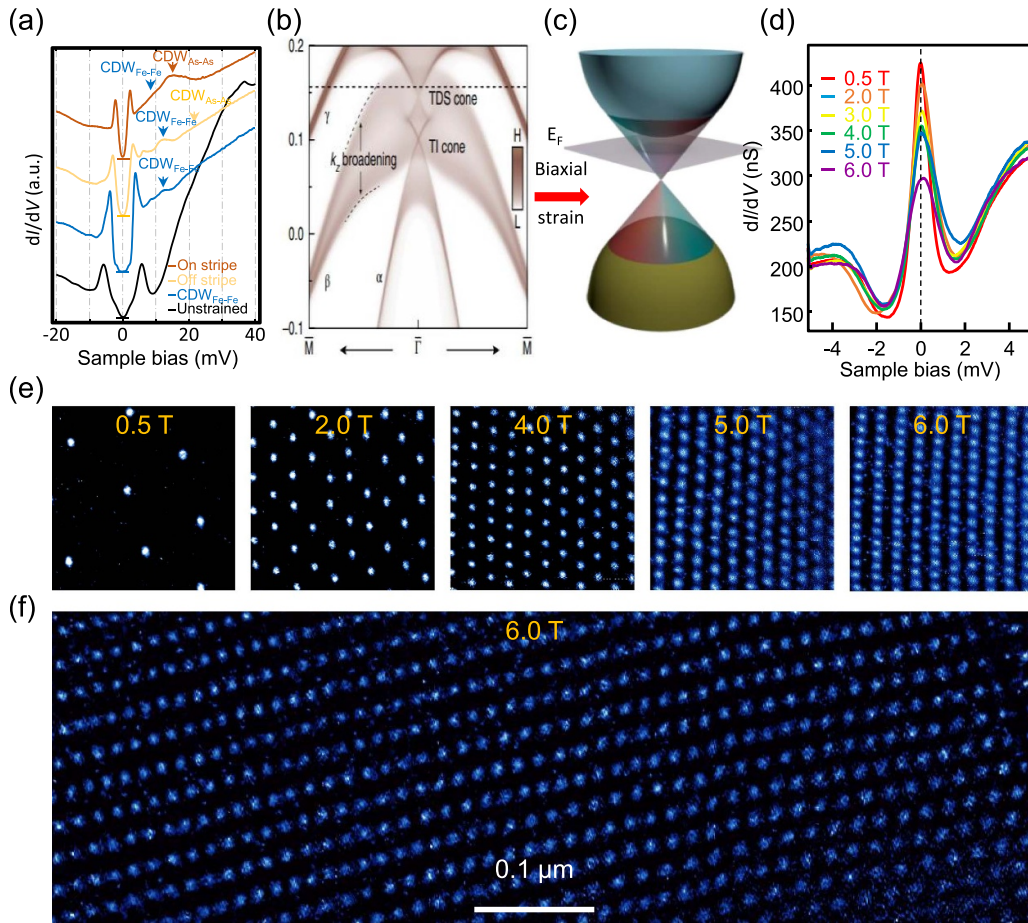


**Figure 15.** Formation of MZM lattice in LiFeAs biaxial charge density wave region. (a) Wide-range  $dI/dV$  spectra at the on As–As stripe (brown) and off As–As stripe (yellow) locations in a biaxial CDW region, the uniaxial  $CDW_{Fe-Fe}$  region (blue), and the unstrained region (black), respectively. (b) (001)-projected surface bands of unstrained LiFeAs. (c) Schematic of the band structure of the strained LiFeAs around the  $\Gamma$  point. (d) Averaged  $dI/dV$  spectra under different magnetic fields. (e) Series of zero energy  $dI/dV$  maps of the MZM vortices in the biaxial CDW region under magnetic fields of 0.5 T, 2 T, 4 T, 5 T and 6 T. (f) Micrometer-sized ordered MZM lattice under 6 T. Adapted from [42], with permission from Springer Nature.

CdGM states are observed inside such vortices (figures 14(b)–(d)). Under higher magnetic field, the pinning effect allows formation of an ordered vortex lattice (figure 14(e)). They have shown that more than 90% of the vortex centers have MZMs (figures 14(f)–(h)), forming an ordered MZM lattice.

Different from the impurities, the biaxial CDW affects the system in two ways. Firstly, as described above, the periodic stripes force the formation of ordered vortex lattice, which is rarely seen in the IBSs. Secondly, it breaks the rotation and mirror symmetries of the system and gaps out the TDS cone into surface Dirac bands (figures 15(a)–(c)). As a result, stable topological vortex lattice is generated and can be tuned by external magnetic field (figures 15(d)–(f)). The size of such an MZM lattice can be up to microns or larger. Therefore, the naturally strained LiFeAs acts as a scalable and tunable platform for topological quantum computation [143].

## 6. Conclusion and perspective

The past several years has witnessed a surge in the MZM-hosting materials. Here, we summarize some of such materials studied by STM/S in table 1. The platform types are generally classified into the bulk type, (2D) film type and the hybrid (structure) type, and the topological defects are classified into the vortex line, line defect, QAV, DW, atomic chain and the island edge. Among all the platforms, monolayer  $FeTe_{0.5}Se_{0.5}$  shows the highest temperature (24 K) to observe an MZM. Compared with  $FeTe_{0.55}Se_{0.45}$ , LiFeAs has a more homogeneous bulk state, and the strained LiFeAs shows the potential of realizing ordered, uniform and scalable MZM lattice. As discussed above, each platform has its own pros and cons, and not a single platform is even close to be used as a host for topological quantum computation, giving the scalability of materials, the probability in finding MZMs, the difficulty in controlling the topological defects and thus the MZMs, and



**Table 1.** MZM platforms experimentally studied by STM/S. The fabrication method, topological defect and the MZM observation temperature are summarized.

Material	Growth method	Platform type	Topological defect	Quasiparticle type	MZM temp.	References
FeTe <sub>x</sub> Se <sub>1-x</sub>	Self-flux	Bulk	Vortex line	MZM	3.3 K	[39]
(Li <sub>1-x</sub> Fe <sub>x</sub> )OHFeSe	Hydrothermal	Bulk	Vortex line	MZM	0.4 K	[40]
Strained LiFeAs	Self-flux	Bulk	Vortex line	MZM	0.4 K	[42]
CaKFe <sub>4</sub> As <sub>4</sub>	Self-flux	Bulk	Vortex line	MZM	0.4 K	[57]
Impurity/LiFeAs	Self-flux	Bulk	Vortex line	MZM	0.4 K	[58]
Fe/FeTe <sub>x</sub> Se <sub>1-x</sub>	MBE	Bulk	QAV	MZM	0.4 K	[59]
FeTe <sub>x</sub> Se <sub>1-x</sub> /STO	MBE	Film	Line defect	MZM	24 K	[60]
FeTe <sub>x</sub> Se <sub>1-x</sub> DW	Self-flux	Bulk	DW	Dispersing	0.3 K	[61]
Fe/Pb(110)	MBE	Hybrid	Fe Chain	MZM	1.4 K	[37]
Bi <sub>2</sub> Te <sub>3</sub> /NbSe <sub>2</sub>	MBE	Hybrid	Vortex line	MZM	0.4 K	[38]
Fe/Re(0001)-O	MBE	Hybrid	Island edge	Dispersing	0.36 K	[47]
CrBr <sub>3</sub> /NbSe <sub>2</sub>	MBE	Hybrid	Island edge	Dispersing	0.35 K	[48]
2M-WS <sub>2</sub>	Deintercalation	Bulk	Vortex line	MZM	0.4 K	[118]
4Hb-TaS <sub>2</sub>	CVT	Bulk	Vortex line/Step edge	Both	0.38 K	[119]
β-Bi <sub>2</sub> Pd	MBE	Film	Vortex line	MZM	0.4 K	[123]

the low temperature needed. As a result, new platforms have to be proposed [144–147] and verified.

Besides the material, new experimental methods and tools should also be implemented in Majorana research. So far, most studies still rely on features such as ZBPs to determine the existence of topological superconductivity, which sometimes causes trouble. Fortunately, we are seeing new local probe tools such as the shot noise spectroscopy come into play. Many more efforts have to be taken to unambiguously verify the existence of MZMs. More importantly, experimental techniques beyond the local probe measurements have to be adopted to confirm the non-Abelian statistics of the MZM array.

### Data availability statement

No new data were created or analyzed in this study.

### Acknowledgments


The work is supported by grants from the Ministry of Science and Technology of China (2019YFA0308500), the National Natural Science Foundation of China (61888102), the Chinese Academy of Sciences (XDB28000000, YSBR-003) and the Innovation Program of Quantum Science and Technology (2021ZD0302700).

### Conflict of interest

The authors declare no competing financial interests.

### ORCID iDs

Geng Li  <https://orcid.org/0000-0002-3347-7222>

Xingtai Zhou  <https://orcid.org/0000-0002-2455-8303>

Hong-Jun Gao  <https://orcid.org/0000-0002-2088-0522>

### References

- [1] Majorana E 1937 *Nuovo Cimento* **14** 171
- [2] Avignone F T, Elliott S R and Engel J 2008 *Rev. Mod. Phys.* **80** 481
- [3] Arnquist I J *et al* 2023 *Phys. Rev. Lett.* **130** 062501
- [4] Qi X L and Zhang S C 2011 *Rev. Mod. Phys.* **83** 1057
- [5] Alicea J 2012 *Rep. Prog. Phys.* **75** 076501
- [6] Kitaev A Y 2003 *Ann. Phys., NY* **303** 2
- [7] Nayak C, Simon S H, Stern A, Freedman M and Das Sarma S 2008 *Rev. Mod. Phys.* **80** 1083
- [8] Beenakker C W J 2013 *Annu. Rev. Condens. Matter Phys.* **4** 113
- [9] Aasen D *et al* 2016 *Phys. Rev. X* **6** 031016
- [10] Moore G and Read N 1991 *Nucl. Phys. B* **360** 362
- [11] Read N and Green D 2000 *Phys. Rev. B* **61** 10267
- [12] Ivanov D A 2001 *Phys. Rev. Lett.* **86** 268
- [13] Kitaev A Y 2001 *Phys.-Usp.* **44** 131
- [14] Maeno Y, Hashimoto H, Yoshida K, Nishizaki S, Fujita T, Bednorz J G and Lichtenberg F 1994 *Nature* **372** 532
- [15] Kallin C 2012 *Rep. Prog. Phys.* **75** 042501
- [16] Hassinger E, Bourgeois-Hope P, Taniguchi H, de Cotret S R, Grissonnanche G, Anwar M S, Maeno Y, Doiron-Leyraud N and Taillefer L 2017 *Phys. Rev. X* **7** 011032
- [17] Ran S *et al* 2019 *Science* **365** 684
- [18] Jiao L, Howard S, Ran S, Wang Z Y, Rodriguez J O, Sigrist M, Wang Z Q, Butch N P and Madhavan V 2020 *Nature* **579** 523
- [19] Pustogow A *et al* 2019 *Nature* **574** 72
- [20] Fu L and Kane C L 2008 *Phys. Rev. Lett.* **100** 096407
- [21] Lutchyn R M, Sau J D and Das Sarma S 2010 *Phys. Rev. Lett.* **105** 077001
- [22] Sau J D, Lutchyn R M, Tewari S and Das Sarma S 2010 *Phys. Rev. Lett.* **104** 040502
- [23] Nadj-Perge S, Drozdov I K, Bernevig B A and Yazdani A 2013 *Phys. Rev. B* **88** 020407
- [24] Braunecker B and Simon P 2013 *Phys. Rev. Lett.* **111** 147202
- [25] Klinovaja J, Stano P, Yazdani A and Loss D 2013 *Phys. Rev. Lett.* **111** 186805
- [26] Li J, Neupert T, Wang Z J, MacDonald A H, Yazdani A and Bernevig B A 2016 *Nat. Commun.* **7** 12297
- [27] Mourik V, Zuo K, Frolov S M, Plissard S R, Bakkers E P A M and Kouwenhoven L P 2012 *Science* **336** 1003



- [28] Pan Y, Nikitin A M, Araizi G K, Huang Y K, Matsushita Y, Naka T and de Visser A 2016 *Sci. Rep.* **6** 28632
- [29] Kolapo A, Li T X, Hosur P and Miller J H 2019 *Sci. Rep.* **9** 12504
- [30] Zhang P *et al* 2019 *Nat. Phys.* **15** 41
- [31] Zhang P *et al* 2018 *Science* **360** 182
- [32] Wang M X *et al* 2012 *Science* **336** 52
- [33] Wilson M N, Hallas A M, Cai Y, Guo S, Gong Z, Sankar R, Chou F C, Uemura Y J and Luke G M 2017 *Phys. Rev. B* **95** 224506
- [34] Neha P, Biswas P K, Das T and Patnaik S 2019 *Phys. Rev. Mater.* **3** 074201
- [35] Sundar S, Gheidi S, Akintola K, Cote A M, Dunsiger S R, Ran S, Butch N P, Saha S R, Paglione J and Sonier J E 2019 *Phys. Rev. B* **100** 140502
- [36] Sharma M M, Sharma P, Karn N K and Awana V P S 2022 *Supercond. Sci. Tech.* **35** 083003
- [37] Nadj-Perge S, Drozdov I K, Li J, Chen H, Jeon S, Seo J, MacDonald A H, Bernevig B A and Yazdani A 2014 *Science* **346** 602
- [38] Xu J P *et al* 2015 *Phys. Rev. Lett.* **114** 017001
- [39] Wang D *et al* 2018 *Science* **362** 333
- [40] Liu Q *et al* 2018 *Phys. Rev. X* **8** 041056
- [41] Zhu S *et al* 2020 *Science* **367** 189
- [42] Li M, Li G, Cao L, Zhou X T, Wang X C, Jin C Q, Chiu C K, Pennycook S J, Wang Z Q and Gao H J 2022 *Nature* **606** 890
- [43] Sun H H *et al* 2016 *Phys. Rev. Lett.* **116** 257003
- [44] Deng M T, Yu C L, Huang G Y, Larsson M, Caroff P and Xu H Q 2012 *Nano Lett.* **12** 6414
- [45] Ruby M, Pientka F, Peng Y, von Oppen F, Heinrich B W and Franke K J 2015 *Phys. Rev. Lett.* **115** 197204
- [46] Kim H, Palacio-Morales A, Posske T, Rozsa L, Palotas K, Szunyogh L, Thorwart M and Wiesendanger R 2018 *Sci. Adv.* **4** eaar5251
- [47] Palacio-Morales A, Mascot E, Cocklin S, Kim H, Rachel S, Morr D K and Wiesendanger R 2019 *Sci. Adv.* **5** eaav6600
- [48] Kezilebieke S, Huda M N, Vano V, Aapro M, Ganguli S C, Silveira O J, Glodzik S, Foster A S, Ojanen T and Liljeroth P 2020 *Nature* **588** 424
- [49] Kezilebieke S *et al* 2021 *Adv. Mater.* **33** 2006850
- [50] Das Sarma S and Pan H N 2021 *Phys. Rev. B* **103** 195158
- [51] Fernandes R M, Coldea A I, Ding H, Fisher I R, Hirschfeld P J and Kotliar G 2022 *Nature* **601** 35
- [52] Li G, Zhu S Y, Wang D F, Wang Y L and Gao H J 2021 *Supercond. Sci. Tech.* **34** 073001
- [53] Li G, Zhu S Y, Fan P, Cao L and Gao H J 2022 *Chin. Phys. B* **31** 080301
- [54] Paglione J and Greene R L 2010 *Nat. Phys.* **6** 645
- [55] Stewart G R 2011 *Rev. Mod. Phys.* **83** 1589
- [56] Wen H H and Li S L 2011 *Annu. Rev. Condens. Matter Phys.* **2** 121
- [57] Liu W Y *et al* 2020 *Nat. Commun.* **11** 5688
- [58] Kong L Y *et al* 2021 *Nat. Commun.* **12** 4146
- [59] Fan P *et al* 2021 *Nat. Commun.* **12** 1348
- [60] Chen C, Jiang K, Zhang Y, Liu C F, Liu Y, Wang Z Q and Wang J 2020 *Nat. Phys.* **16** 536
- [61] Wang Z Y, Rodriguez J O, Jiao L, Howard S, Graham M, Gu G D, Hughes T L, Morr D K and Madhavan V 2020 *Science* **367** 104
- [62] Fleming G T, Kogut J B and Vranas P M 2001 *Phys. Rev. D* **64** 034510
- [63] Zhu Z, Zheng H and Jia J F 2021 *J. Appl. Phys.* **129** 151104
- [64] Val'kov VV, Shustin MS, Aksenov SV, Zlotnikov AO, Fedoseev AD, Mitskan VA and Kagan MY 2022 *Phys.-Usp.* **65** 2
- [65] Prada E, San-Jose P, de Moor M W A, Geresdi A, Lee E J H, Klinovaja J, Loss D, Nygard J, Aguado R and Kouwenhoven L P 2020 *Nat. Rev. Phys.* **2** 575
- [66] Hsu F C *et al* 2008 *Proc. Natl Acad. Sci. USA* **105** 14262
- [67] Shibauchi T, Hanaguri T and Matsuda Y 2020 *J. Phys. Soc. Japan* **89** 102002
- [68] Fernandes R M, Chubukov A V and Schmalian J 2014 *Nat. Phys.* **10** 97
- [69] Wang F, Kivelson S A and Lee D H 2015 *Nat. Phys.* **11** 959
- [70] Yamakawa Y, Onari S and Kontani H 2016 *Phys. Rev. X* **6** 021032
- [71] Ok J M *et al* 2020 *Phys. Rev. B* **101** 224509
- [72] Kasahara S *et al* 2020 *Phys. Rev. Lett.* **124** 107001
- [73] Wang Q Y *et al* 2012 *Chin. Phys. Lett.* **29** 037402
- [74] Hao N N and Hu J P 2014 *Phys. Rev. X* **4** 031053
- [75] Hao N and Hu J P 2019 *Natl Sci. Rev.* **6** 213
- [76] Wang Z J *et al* 2015 *Phys. Rev. B* **92** 115119
- [77] Fang M H, Pham H M, Qian B, Liu T J, Vehstedt E K, Liu Y, Spinu L and Mao Z Q 2008 *Phys. Rev. B* **78** 224503
- [78] Chen G F, Chen Z G, Dong J, Hu W Z, Li G, Zhang X D, Zheng P, Luo J L and Wang N L 2009 *Phys. Rev. B* **79** 140509(R)
- [79] Pourret A, Malone L, Antunes A B, Yadav C S, Paulose P L, Fauque B and Behnia K 2011 *Phys. Rev. B* **83** 020504(R)
- [80] Homes C C, Dai Y M, Wen J S, Xu Z J and Gu G D 2015 *Phys. Rev. B* **91** 144503
- [81] Xu G, Lian B, Tang P Z, Qi X L and Zhang S C 2016 *Phys. Rev. Lett.* **117** 047001
- [82] Zhang Z Y 2017 *Sci. Bull.* **62** 671
- [83] Qin W, Gao J Q, Cui P and Zhang Z Y 2023 *Sci. China Phys. Mech. Astron.* **66** 267005
- [84] Machida T, Sun Y, Pyon S, Takeda S, Kohsaka Y, Hanaguri T, Sasagawa T and Tamegai T 2019 *Nat. Mater.* **18** 811
- [85] Chiu C K, Machida T, Huang Y Y, Hanaguri T and Zhang F C 2020 *Sci. Adv.* **6** eaay0443
- [86] Jack B, Xie Y L and Yazdani A 2021 *Nat. Rev. Phys.* **3** 541
- [87] Law K T, Lee P A and Ng T K 2009 *Phys. Rev. Lett.* **103** 237001
- [88] Ge J F, Bastiaans K M, Chatzopoulos D, Cho D, Tromp W O, Benschop T, Niu J, Gu G and Allan M P 2022 (arXiv:2205.10346)
- [89] Yu L 1965 *Acta Phys. Sin.* **21** 75
- [90] Shiba H 1968 *Prog. Theor. Phys.* **40** 435
- [91] Rusinov A I 1969 *JETP Lett.* **9** 1101
- [92] Caroli C, De Gennes P G and Matricon J 1964 *Phys. Lett.* **9** 307
- [93] Jeon S, Xie Y L, Li J, Wang Z J, Bernevig B A and Yazdani A 2017 *Science* **358** 772
- [94] Wang D F, Wiebe J, Zhong R D, Gu G D and Wiesendanger R 2021 *Phys. Rev. Lett.* **126** 076802
- [95] Lu X F *et al* 2015 *Nat. Mater.* **14** 325
- [96] Huang Y L *et al* 2017 *Chin. Phys. Lett.* **34** 077404
- [97] Hayashi N, Isoshima T, Ichioka M and Machida K 1998 *Phys. Rev. Lett.* **80** 2921
- [98] Khaymovich I M, Kopnin N B, Mel'nikov A S and Shereshevskii I A 2009 *Phys. Rev. B* **79** 224506
- [99] Hu L H, Li C, Xu D H, Zhou Y and Zhang F C 2016 *Phys. Rev. B* **94** 224501
- [100] Kong L *et al* 2019 *Nat. Phys.* **15** 1181
- [101] Chen C, Liu Q, Zhang T Z, Li D, Shen P P, Dong X L, Zhao Z X, Zhang T and Feng D L 2019 *Chin. Phys. Lett.* **36** 057403
- [102] Zhang Y, Jiang K, Zhang F C, Wang J and Wang Z Q 2021 *Phys. Rev. X* **11** 011041
- [103] Yin J X *et al* 2015 *Nat. Phys.* **11** 543

- [104] Hu J P 2013 *Phys. Rev. X* **3** 031004
- [105] Hao N N and Hu J P 2014 *Phys. Rev. B* **89** 045144
- [106] Cao L *et al* 2021 *Nano Res.* **14** 3921
- [107] Iyo A, Kawashima K, Kinjo T, Nishio T, Ishida S, Fujihisa H, Gotoh Y, Kihou K, Eisaki H and Yoshida Y 2016 *J. Am. Chem. Soc.* **138** 3410
- [108] Kawakami T and Hu X 2015 *Phys. Rev. Lett.* **115** 177001
- [109] Wang X C, Liu Q Q, Lv Y X, Gao W B, Yang L X, Yu R C, Li F Y and Jin C Q 2008 *Solid State Commun.* **148** 538
- [110] Yin J X *et al* 2019 *Phys. Rev. Lett.* **123** 217004
- [111] Hanaguri T, Kitagawa K, Matsubayashi K, Mazaki Y, Uwatoko Y and Takagi H 2012 *Phys. Rev. B* **85** 214505
- [112] Hu L H, Wu X X, Liu C X and Zhang R X 2022 *Phys. Rev. Lett.* **129** 277001
- [113] Konig E J and Coleman P 2019 *Phys. Rev. Lett.* **122** 207001
- [114] Qin S S, Hu L H, Le C C, Zeng J F, Zhang F C, Fang C and Hu J P 2019 *Phys. Rev. Lett.* **123** 027003
- [115] Zheng H and Jia J F 2019 *Chin. Phys. B* **28** 067403
- [116] Chen M Y, Chen X Y, Yang H, Du Z Y and Wen H H 2018 *Sci. Adv.* **4** eaat1084
- [117] Liang J, Zhang Y J, Yao X, Li H, Li Z X, Wang J N, Chen Y Z and Sou I K 2020 *Proc. Natl Acad. Sci. USA* **117** 221
- [118] Yuan Y H *et al* 2019 *Nat. Phys.* **15** 1046
- [119] Nayak A K *et al* 2021 *Nat. Phys.* **17** 1413
- [120] Noh H J, Jeong J, Cho E J, Kim K, Min B I and Park B G 2017 *Phys. Rev. Lett.* **119** 016401
- [121] Zheng F P, Li X B, Lin Y P, Xiong L X, Chen X B and Feng J 2020 *Phys. Rev. B* **101** 100505
- [122] de Lima B S, de Cassia R R, Santos F B, Correa L E, Grant T W, Manesco A L R, Martins G W, Eleno L T F, Torikachvili M S and Machado A J S 2018 *Solid State Commun.* **283** 27
- [123] Lv Y F, Wang W L, Zhang Y M, Ding H, Li W, Wang L L, He K, Song C L, Ma X C and Xue Q K 2017 *Sci. Bull.* **62** 852
- [124] Wray L A, Xu S Y, Xia Y Q, Hor Y S, Qian D, Fedorov A V, Lin H, Bansil A, Cava R J and Hasan M Z 2010 *Nat. Phys.* **6** 855
- [125] Tao R, Yan Y J, Liu X, Wang Z W, Ando Y, Wang Q H, Zhang T and Feng D L 2018 *Phys. Rev. X* **8** 041024
- [126] Tanaka Y *et al* 2012 *Phys. Rev. B* **85** 125111
- [127] Liu Z H, Yao X, Shao J F, Zuo M, Po L, Tan S, Zhang C J and Zhang Y H 2015 *J. Am. Chem. Soc.* **137** 10512
- [128] Du G *et al* 2017 *Nat. Commun.* **8** 14466
- [129] Han C Q *et al* 2015 *Appl. Phys. Lett.* **107** 171602
- [130] Sharma M M, Rani P, Sang L N, Wang X L and Awana V P S 2020 *J. Supercond. Nov. Magn.* **33** 565
- [131] Sirohi A, Das S, Neha P, Jat K S, Patnaik S and Sheet G 2018 *Phys. Rev. B* **98** 094523
- [132] Wang Y, Sato H, Toda Y, Ueda S, Hiramatsu H and Hosono H 2014 *Chem. Mater.* **26** 7209
- [133] Sharma M M, Karn N K, Sharma P, Gurjar G, Patnaik S and Awana V P S 2021 *Solid State Commun.* **340** 114531
- [134] Liu B, Xiao C C, Zhu Q Q, Wu J F, Cui Y W, Wang H D, Wang Z C, Lu Y H, Ren Z and Cao G H 2019 *Phys. Rev. Mater.* **3** 084603
- [135] Sharma M M, Sharma P, Gurjar G, Patnaik S and Awana V P S 2021 *J. Phys. Chem. Solids* **156** 110136
- [136] Khim S *et al* 2021 *Science* **373** 1012
- [137] Landaeta J F *et al* 2022 *Phys. Rev. X* **12** 031001
- [138] Ortiz B R *et al* 2020 *Phys. Rev. Lett.* **125** 247002
- [139] Chen H *et al* 2021 *Nature* **599** 222
- [140] Liang Z W *et al* 2021 *Phys. Rev. X* **11** 031026
- [141] Cao L *et al* 2021 *Nat. Commun.* **12** 6312
- [142] Yim C M, Trainer C, Aluru R, Chi S, Hardy W N, Liang R X, Bonn D and Wahl P 2018 *Nat. Commun.* **9** 2602
- [143] Bonderson P, Freedman M and Nayak C 2009 *Ann. Phys., NY* **324** 787
- [144] Wang Y X, Lin M and Hughes T L 2018 *Phys. Rev. B* **98** 165144
- [145] Wang Q Y, Liu C C, Lu Y M and Zhang F 2018 *Phys. Rev. Lett.* **121** 186801
- [146] Hsu C H, Stano P, Klinovaja J and Loss D 2018 *Phys. Rev. Lett.* **121** 196801
- [147] Li C, Luo X J, Chen L, Liu D E, Zhang F C and Liu X 2022 *Natl Sci. Rev.* **9** nwac095